Curve Parametric Modeling of Planar Soft Robots

Dulanjana M. Perera
Dept. of Multidisciplinary Engineering
Texas A&M University
College Station, Texas, USA
dperera@tamu.edu

Nathan Byrd
Dept. of Mechanical Engineering
Texas A&M University
College Station, Texas, USA
ncbyrd@tamu.edu

Dimuthu D. K. Arachchige
School of Computing
DePaul University
Chicago, Illinois, USA
darachch@depaul.edu

Bhaskar Vajipeyajula
Dept. of Eng. Tech. & Ind. Distribution
Texas A&M University
College Station, Texas, USA
vaji19@tamu.edu

Kevin C. Galloway
Dept. of Mechanical Engineering
Vanderbilt University
Nashville, Tennessee, USA
kevin.c.galloway@vanderbilt.edu

Isuru S. Godage
Dept. of Eng. Techn. & Ind. Distribution
Texas A&M University
College Station, Texas, USA
igodage@tamu.edu

***Abstract*—Soft robots, due to their flexibility, adaptability, and gentle handling over rigid robots, have shown better potential in numerous applications requiring operating in constrained spaces. Most of the soft robotic prototypes are of a linear form that can be modeled as a curve in space and are found in manipulators and limbs of locomoting robots. Planar soft robots have been proposed recently that are modeled as a surface and deform in 3D. Research on planar soft robots has been less extensive due to the challenges associated with modeling surface deformations efficiently. We present a curve-parametric approach for the deformation modeling of planar soft robot modules. Along with the Bezier patch method to approximate the surface at 30 Hz. Experimental evaluations on a prototype were developed and tested to validate that the proposed model can reasonably approximate the planar robot boundaries and the surface derived from it.**

***Index Terms*—surface modeling, curve parametric, Bezier surface, planar robots, soft robots.**

I. Introduction

Soft robots, comprising compliant materials, exhibit a unique ability to navigate constrained environments and interact delicately with objects, making them well-suited for tasks requiring dexterity and adaptability than their rigid counterparts [1]. Through the integration of advanced materials and innovative actuation mechanisms, soft robots offer promising advancements in various fields, including biomedical engineering, industrial automation, and human-robot interaction [2].

Soft robots, particularly those featuring a linear arrangement of actuators inspired by the dexterity and versatility of tentacles and elephant trunks, demonstrate remarkable capabilities in navigating tight spaces and handling delicate objects, embodying the potential for advancements in fields requiring fine manipulative skills and adaptive interaction [3]. Examining natural biological examples like the fins of Rajiformes, one can observe deforming planar structures. In these systems, deformation occurs from internal musculature and across the entire surface. Surface structures, compared to tentacle-like structures, can generate complex shapes. This prompts an inquiry into employing soft surface robots to emulate these biological structures for various tasks such as compliant manipulation and locomotion, adaptable wing structures, and wearable systems.

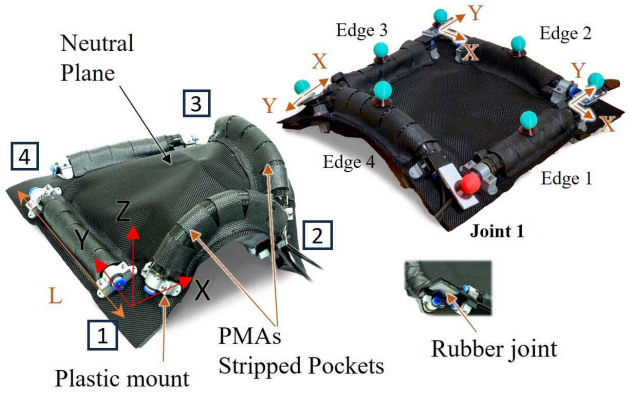

Fig. 1. Planar soft module shapes. The number indicates the corresponding joint. The robot coordinate frame is placed at Joint-1. The neutral plane is the non-stretchable fabric. Pneumatic Muscle Actuators (PMAs) are used to actuate the system. The pockets are striped to facilitate the bending of the PMAs. Marker placement on the planar robot. The red marker is considered to be the origin of the tracker system

Suzumori et al. utilized a pneumatic surface actuator for propelling an underwater soft robot [4]. Cai et al. powered a robotic fish utilizing deforming fins but mathematical models were not proposed [5]. Deng et al., inspired by a caterpillar, introduced a soft machine table for object manipulation [6]. Therein, a discrete piece-wise approach was employed to delineate the curvature of each unit on the table. Authors in [7] presented a structure operated by shape memory alloy wires where the kinematics of the mechanism used a grid-based technique. While these systems demonstrated considerable deformability, they incorporated predominantly rigid/semi-rigid components in the design, thereby lacking smooth and continuous deformation. Addressing this, authors in [8] utilized finite element analysis to study composite laminates in continuum robot applications, though it is hampered by computational intensity.

Kirchhoff-Love and Cosserat plate theories can be utilized to examine the deformation of soft surfaces [9]. Kano et al. proposed a continuous model for a sheet-like robot, which was verified only through simulation [10]. Merino et al. presented an interpolation technique to model the curvature of edges on a continuous surface [11]. Watanabe et al. applied wave propagation theory to manipulate flexible sheet actuators [12]. These models focus solely on the surface geometry and do not capture the actuator-surface inter-connectivity.

The lumped-mass approach, which involves discretely approximating the soft surface, has been proposed to model planar surface soft robots [13]. The complexity of this modeling approach presents challenges when implementing efficient modeling and control strategies. On the other hand, the curve parametric approach for modeling soft robots is simple yet offers increased efficiency due to its ability to capture the geometrical complexities associated with large deformations of continuum arms [14]–[16]. Moreover, it enables a more intuitive and flexible design process, facilitating the optimization of soft robot geometries for specific tasks and applications. The efficient nature of curve parametric modeling contributes to enhancing the design, control, and overall functionality.

In this work, we introduce curve parametric modeling for a planar surface robot, enhancing the design and functionality of soft robots by allowing accurate control over complex surface deformations. Our specific technical contributions include:

i. Design and fabricate a planar soft continuum module with Pneumatic Muscle Actuators (PMA) and non-stretchable fabric to obtain surface-like deformation.
ii. Apply curve parametric approach to obtain an efficient kinematic model for bending planar soft module edge actuators. By using curves to describe the movement of the actuators, this approach captures the complex and continuous deformations of the soft robot more effectively.
iii. Model the soft planar robot surface using Bezier patches for efficient surface estimation. Bezier patches offer a flexible and computationally efficient method for representing complex surfaces, allowing for more accurate simulations.
iv. Experimentally validate the kinematic model that uses novel surface curve parameters to model planar soft robots.

II. Prototype Description

A. Prototype Design

The proposed planar module in this study deforms like a rubber sheet when unpowered, and has the structural rigidity to actively deform when actuated. It is constructed from strategically placed stiffer materials as well as soft materials (see Fig. 1). It employs non-stretchable fabric (Neutral plane) with PMAs at the edges [17]. The PMA and the joints provide structural rigidity while the fabric facilitates flexibility as well as provides mechanical constraints to the system needed to generate controllable deformations. The PMAs are arranged in a square configuration, as depicted in Fig. 1. They are placed antagonistically to ensure planar bidirectional bending. The pocket surrounding the PMA confines and mitigates buckling

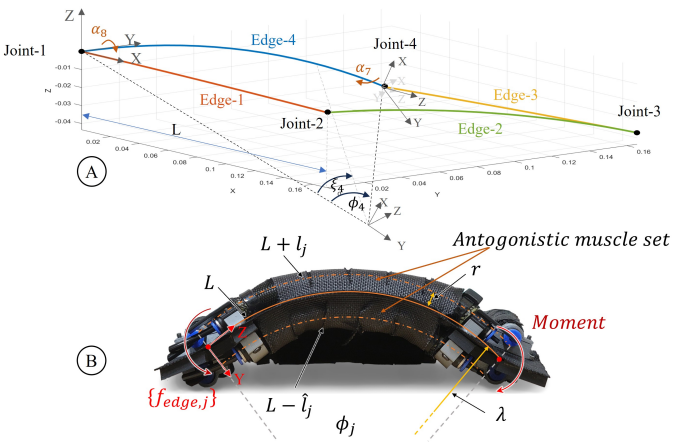

Fig. 2. System Kinematics. (A) The colored-solid lines illustrate the neutral axis at each edge. The α_7 and α_8 designate the twist around the *y-axis* of the global coordinate frame. (B) An illustration of bending due to the extension of PMA. The unbalanced moment at the anchor points causes the bending. The $f_{edge,j}$ is the actuator frame, l_j is the extension of the PMA_j, r, and λ is offset from the neutral plane and radius of the arc, respectively. The $\hat{l}_j = l_j$ from (1).

to ensure smooth and continuous deformation. These pockets are striped to emulate the stretching effect and facilitate the extension required for the PMA.

PMAs, anchored at both ends, induces an unbalanced moment on the fabric surface (neutral plane), thereby resulting in the desired planar bending (Fig. 2B). The pocket constrains the PMA to a planar bending and ensures uniform curvature. Bi-directional bending is achieved by affixing an additional antagonistic PMA on the underside of the fabric. This PMA pair arrangement is replicated at the four edges of the sqauare pattern. A rubber joint (Fig. 1) interconnects each muscle pair, adding an additional passive DoF to the system which allows them to rotate about their longitudinal axes (i.e., $\alpha_{7,8}$ in Fig. 2A) and thereby bend out-of-plane when constrained. The 3D printed anchor joints clamp around the quick-disconnect fittings of PMAs and secure to the inextensible fabric via metal bolts. During operation, the anchor joints and the fabric restrict PMA extension that causes bending (Fig 2B). These anchor joints at both ends of PMA pairs ensure co-planarity, thereby upholding system balance.

B. System Characterization

We model the deformation of the neutral plane of the planar soft robot shown in Fig. 2. The configuration $\mathbf{C} : \{\Phi, \alpha_i \in \mathbb{R}^4 : -\pi \leq \phi \leq \pi\}$ where $\Phi = [\phi_1 \ \phi_2 \ \phi_3 \ \phi_4]^T$ is the bending angle vector of four edges (Antagonistic Muscle Set (AMS)), and α_i $i \in \{1, 2, ..., 8\}$ is the joint rotation. The task space is defined as $\mathbf{X} : \{R \in \mathbb{R}^3\}$ where R is the selected point on the robot's edge in Cartesian space. The unbalanced moment occurs due to the 17 *mm* offset of the PMA center line from the neutral plane as illustrated in Fig. 2B. By utilizing this, we can derive a joint space-configuration space map as follows.

$$L \pm l_j = (\lambda \pm r)\,\phi_i = \left(\frac{L}{\phi_j} \pm r\right)\phi_i$$
$$l_j = r\phi_j \tag{1}$$

where $r \in \mathbb{R}$ is the offset and $\lambda \in \mathbb{R}$ is the radius of the bending arc with Note that even though AMS has two actuators, the system exhibits a single DoF which is bi-directional bending. The actuator-joint space relationship (i.e., pressure-length) is obtained experimentally (see Fig. 3) and approximated by,

$$l_j = (5.25p_j^4 - 35.69p_j^3 + 73.69p_j^2 - 22.56p_j + 1.36)10^{-3} \tag{2}$$

where $p_j \in [0,3]$ *bar* is the pressure of the PMA muscle. Therefore by combining (1) and (2), we can derive the following relationship for ϕ_j,

$$\phi_j = \tfrac{1}{10^3 r}\left(5.25p_j^4 - 35.69p_j^3 + 73.69p_j^2 - 22.56p_j + 1.36\right) \tag{3}$$

Note that, in this article, we do not validate the configuration-actuator space relation. However, we present the derivation for completeness. The following section presents the experimental validation of the kinematic model in task space.

III. System Model

A. Modeling of Surface Boundary

The base coordinate frame is placed at the first joint on the neutral plane, as illustrated in Fig. 1. The *z-axis* is pointed upward and the *x-axis* is aligned with the edge-1. A single actuator kinematic is derived as presented in (4). In the derivation, we defined a convention such that, the actuator frame is rotated to align the z-axis with the edge and the y-axis is perpendicular to the neutral plane (see Fig. 2B). The kinematic model of a j-th AMS is presented in (4).

$$T_{AMS,j} = T_y(L/\phi_j)\cdot R_x(\pi/2 - \xi_j\phi_j)\cdot T_z(L/\phi_j)\cdot R_x^T(\pi/2) \tag{4}$$

where $\xi_j = [0,1]$ is a selection factor of j-th AMS to select a point along the AMS. Therefore, $\xi_j = 0$ is for the base of the j-th AMS, and $\xi_j = 1$ is for the tip of the j-th AMS. The L/ϕ denotes the radius, λ_j of the circular arc.

The AMS and its arrangement in the proposed design make it a closed-chain robot. Therefore, singularities and multiple

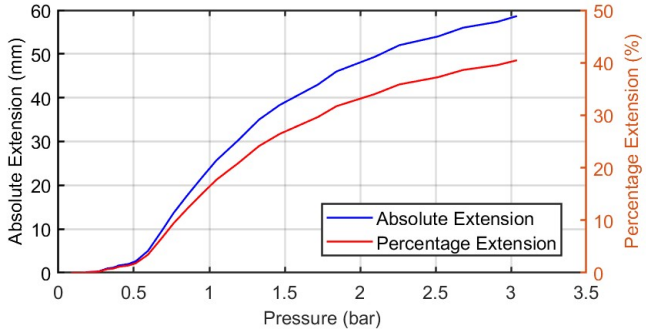

Fig. 3. A single PMA extension l_j with pressure (average of 5 trials.)

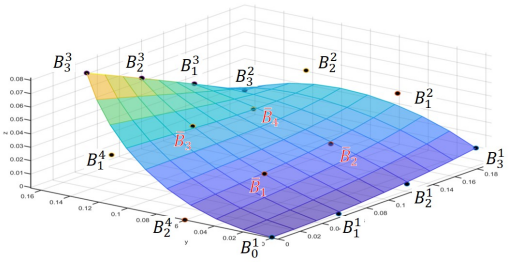

Fig. 4. Boundary Control points and the interpolated control points

solutions for forward kinematics can be anticipated. In (4), a singularity can be observed when $\phi_j = 0$. Thus the range of Φ can be defined as $\phi_j \in [-\pi,\pi]$ where $\phi_j \neq 0$. The loop closure constraints are employed to derive the close-loop kinematics of the system and two forward kinematic equations are derived for the joint-3. The first equation T_{123} for the loop is defined through joint-1 $\rightarrow$ joint-2 $\rightarrow$ joint-3, and the second, T_{143} is defined as joint-1 $\rightarrow$ joint-4 $\rightarrow$ joint-3. Utilizing the $T_{AMS,j}$, the homogeneous transformation, T_{123} and T_{143} are given in (6), and (5).

$$T_{143} = R_x^T(\pi/2)\cdot R_z(\alpha_8)\cdot T_{AMS,4}\cdot R_z(\alpha_7)\cdot R_y(\pi/2)\cdot R_z(\alpha_6)\cdot T_{AMS,3}\cdot R_z(\alpha_5)\cdot R_x(\pi/2) \tag{5}$$

$$T_{123} = R_z^T(\pi/2)\cdot R_x^T(\pi/2)\cdot R_z(\alpha_1)\cdot T_{AMS,1}\cdot R_z(\alpha_2)\cdot R_y^T(\pi/2)\cdot R_z(\alpha_3)\cdot T_{AMS,2}\cdot R_z(\alpha_4)\cdot R_x(\pi/2) \tag{6}$$

Here, $\alpha = \{\alpha_k \in \mathbb{R} \mid k = 1,2,..7,8\}$ represent the joint rotations. In (5), initial $Rx\left(-\frac{\pi}{2}\right)$ is applied to align the *z-axis* with the AMS-4. In (6), the base frame has to be rotated around *z-axis* and rotated around *x-axis* to align the *z-axis* with the AMS-1.

However, the α_i is unknown, and *Interior-point* constraint optimization is followed to obtain the solutions for the given ϕ_j. Since the position vectors of T_{123} and T_{143} refer to the same position, the following cost function is defined for the constrained minimization.

$$f(\alpha) = [P_{123}(\alpha) - P_{143}(\alpha)]^T [P_{123}(\alpha) - P_{143}(\alpha)] \tag{7}$$

where P_{123} is the position vector of the T_{123} and P_{143} is that of T_{143}. Note that P_{123} is a function of Φ, ξ, and α. However, for simplicity, we only state α due to the relevancy of the optimization. Then, the optimization problem can be defined as follows with constraints.

$$\alpha_k^* = \begin{cases} \min f(\alpha_k) \\ -\frac{\pi}{2} \leq \alpha_k \leq \frac{\pi}{2} \quad k = \{1,2,...,8\} \end{cases} \tag{8}$$

where α_k^* is the optimum rotational angle for given Φ. The forward kinematic of the tip of each muscle is given as

$$X_{AMS,1} = P_{123}(\Phi, \alpha^*, \xi_1 = 1, \xi_2 = 0) \tag{9a}$$
$$X_{AMS,2} = P_{123}(\Phi, \alpha^*, \xi_1 = 1, \xi_2 = 1) \tag{9b}$$
$$X_{AMS,3} = P_{143}(\Phi, \alpha^*, \xi_4 = 1, \xi_3 = 1) \tag{9c}$$
$$X_{AMS,4} = P_{143}(\Phi, \alpha^*, \xi_4 = 1, \xi_3 = 0) \tag{9d}$$

B. Modeling of the Surface

We use cubic Bezier surface approach to model the neutral surface bounded by the 4 AMS due to efficiency and resulting smooth surface [18]. A cubic Bezier curve is given by

$$q_{AMS,j}(u) = (1-u)^3 B_0^j + 3u(1-u)^2 B_1^j + 3u^2(1-u)B_2^j + u^3 B_4^j \quad (10)$$

where, $q_{AMS,j}(u)$ is the parametric curve function of the j^{th} AMS, and $u = [0,\ 1]$ is the selection parameter along the curve. The B_k^j is the k^{th} control point of the j^{th} curve. When $u = 0$, the curve selects the B_0^j, the initial point, and when $u = 1$, it selects, B_3^j.

One challenge in this approach is that the control points of the surface have to be derived from the boundary curves. In addition, the surface needs intermediate curves to define the shape. To address this, we initially, approximate the Bezier control points for the boundary curves. To that end, we use the least-square curve fitting approach as it is an efficient method to fit a curve [19]. The error function is defined with the boundary curve data points for the least-square fitting as

$$E_j = \sum_{u=0}^{100} \left[s_{AMS,j}(u) - q_{AMS,j}(u) \right]^2 \quad (11)$$

where $s_{AMS,j}(u)$ is the discretized u^{th} point of j^{th} AMS. Here, we discretize the boundary curve into 100 points. To minimize the error between data points, the following condition denoted by (12) has to be met.

$$B_0^j = s_{AMS,j}(0),\ B_3^j = s_{AMS,j}(100),\ \frac{\partial E}{\partial B_1^j} = 0,\ \frac{\partial E}{\partial B_2^j} = 0 \quad (12)$$

By solving the (12), we can get the B_1^j, and B_2^j that approximate the the $s_{AMS,j}$. Then, to obtain the intermediate control points between two parallel boundary curves, interpolation is considered i.e., the (13) defines the intermediate control points.

$$\begin{aligned} \bar{B}_1 &= (2B_1^1 + B_1^2 + B_2^3 + 2B_2^4)/6 \\ \bar{B}_2 &= (2B_2^1 + 2B_1^2 + B_1^3 + B_2^4)/6 \\ \bar{B}_3 &= (B_1^1 + B_2^2 + 2B_2^3 + 2B_1^4)/6 \\ \bar{B}_4 &= (B_2^1 + 2B_2^2 + 2B_1^3 + B_1^4)/6 \end{aligned} \quad (13)$$

The $2/3$ and $1/3$ weights are given according to the closeness of the new point ($\bar{B}_k$) to the boundary control points (B_*^j) (see Fig. 4). For example, a boundary point close to the new point is given $2/3$. These Control points are used to obtain the Bezier surface. The control points are arranged in grid format to use in the following mathematical definition.

$$Surface = \sum_{c_x=0}^{3} \sum_{c_y=0}^{3} BP_{c_x}(u) BP_{c_y}(v) \hat{P}_{c_x,c_y} \quad (14)$$

where,

$$BP_{c_x}(u) = \left(\frac{3!}{c_x!(3-c_x)!} \right) u^{c_x} (1-u)^{3-c_x}$$

$$BP_{c_y}(v) = \left(\frac{3!}{c_y!(3-c_y)!} \right) v^{c_y} (1-v)^{3-c_y}$$

is the Bernstein polynomials. Here $\hat{P}_{c_x,c_y} \in \mathbb{R}^{4\times4}$ is the matrix of all the control points, and $c_x,\ c_y$ are the index of the matrix.

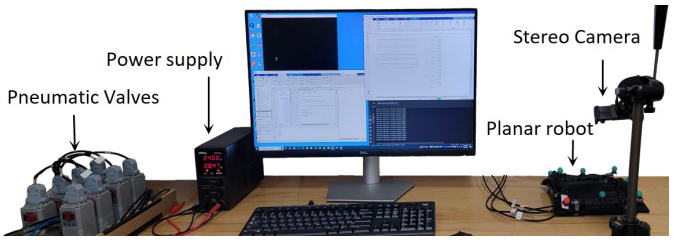

Fig. 5. Experimental setup

IV. Experimental Validation

A. Experimental Setup

A motion tracking system is used to measure the selected points on the surface of the robot, whereas IMUs (MPU 9250) are utilized to measure the bending angle (ϕ_j) of each AMS. The pneumatic air is controlled by 8 proportional control solenoid values (1700 Series, Pneumax). To track the deflection angle of the actuators, 3 IMUs were fitted to joints 2, 3, and 4 as depicted in Fig. 1. The x-orientation of IMU 1 measures the angle of ϕ_1 in addition to IMU 2 measures the angle of ϕ_3. The y-orientation of both IMU 1 and 2 captures the ϕ_2 whereas IMU 3 measures the angle of ϕ_4. Note that IMU only measures the angle $\phi_j/2$. A visual demonstration of the robot can be found here https://youtu.be/-E7g2KndsfI.

Camera tracking is implemented to measure the shape of the AMS. After calibration, the origin is initialized at joint 1 (where the red tracker is mounted). The robot was approximately aligned to the camera coordinate frame, and minor corrections were made by performing coordinate alignment. Following a clockwise motion, a tracker is fitted to every joint and center of each actuator equidistant to their respective joints as in Fig. 1. The trackers are mounted on top of the AMS, though the simulation is derived for the neutral plane. Therefore, an offset correction 17 *mm*, was performed to project the tracker to the neutral plane. To obtain the projection direction, especially when the bending occurs, IMU data is utilized to procure the binomial direction towards the positive curvature. The tracking points are aligned and compared with the simulation results to validate the accuracy of the proposed model. The bending angles obtained from the experiments were used in the simulation.

B. Convex Bending

The experiments were conducted by applying 0.5 - 3 bars of constant air pressure using MATLAB individually to the actuators, causing the AMS to bend. Make note that in Fig. 3, it is evident the deadzone of the PMA is 0.5 *bar*. In Fig. 6, a comparison is made between the actual robot as deflection occurs and the simulation shape during the positive bending. The experiment is conducted to show the accuracy of the model's estimation for single AMS actuation in positive bending.

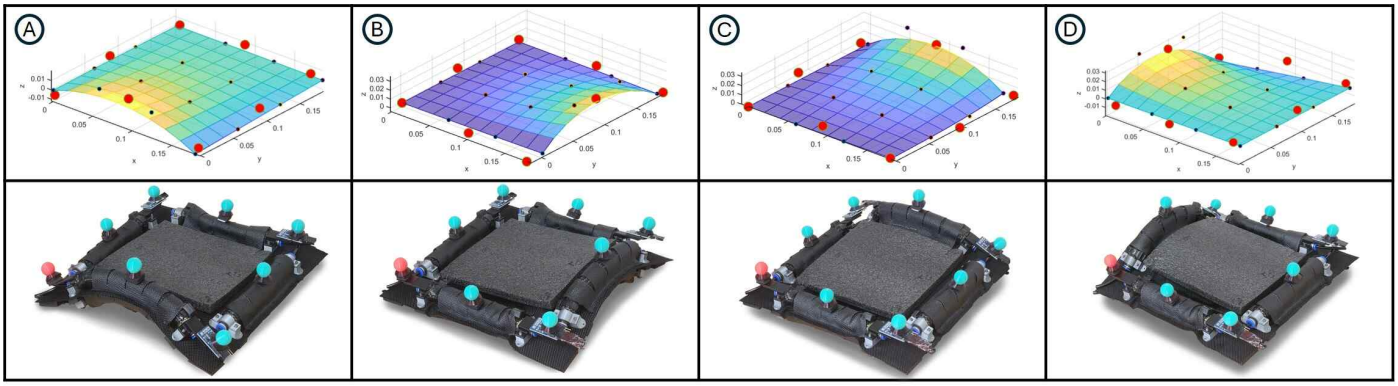

Fig. 6. Actual and simulation results of convex bending (Positive bending). The red dots in the simulation figures indicate the actual position of the robot (red and green markers). The black dots indicates the Bezier curve's control points. (A) AMS_1 bending at $\phi_1 = 0.785$, (B) AMS_2 bending at $\phi_2 = 1.176$, (C) AMS_3 bending at $\phi_3 = 1.159$, (D) AMS_4 bending at $\phi_4 = 1.299$

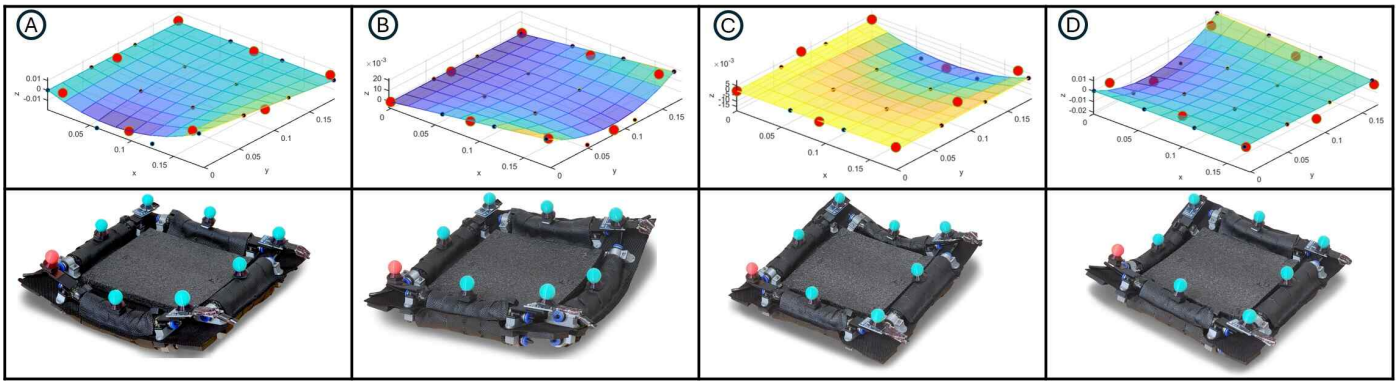

Fig. 7. Actual and simulation results of concave bending (Negative bending). (A) AMS_1 bending at $\phi_1 = -0.778$, (B) AMS_2 bending at $\phi_2 = -0.876$, (C) AMS_3 bending at $\phi_3 = -0.611$, (D) AMS_4 bending at $\phi_4 = -0.939$

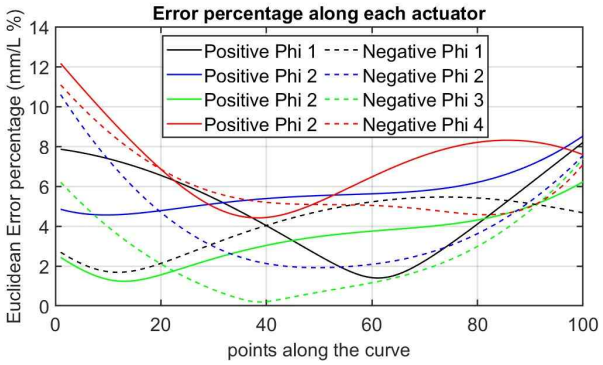

Fig. 8. Error percentage of each experiment with respect to the actuator length, 175 *mm* (error/Length).

C. Concave Bending

Figure 7 indicates negative bending experiments that have a similar performance as the convex (positive) bending. This indicates that model performance remains unchanged when a single AMS is actuated and independent of the bending direction. It is evident in the error plot presented in Fig. 8. The error along the bending curve is presented wherein the error percentage is computed for the AMS length (175 *mm*). The model closely resembles the actual robot's shape with a maximum 12% error. This error is mainly observed in AMS 2 and 4. When the robot bends one AMS, it contracts the adjacent AMS. This phenomenon is partially exhibited in the model. However, the misrepresentation is minimal when a single AMS is actuated.

D. Mixed bending shapes

Figure 9 shows how the model computes the shape when multiple AMS are actuated simultaneously. The results show that the model has a challenge when representing the kinematics. During the multiple actuations, module behavior is affected by gravity resulting in orientation changes. The dynamic effects are not accounted for in the kinematic model. However, the overall representation of the surface is below 12%.

Compared to the existing planar soft module in [13], the proposed system can bend all four edges bi-directionally (see Fig. 10). The [13] only has two parallel actuators and the shapes the module demonstrated only either convex or concave shapes. The proposed system can perform mixed bending shapes resulting in more complicated and smoother surfaces

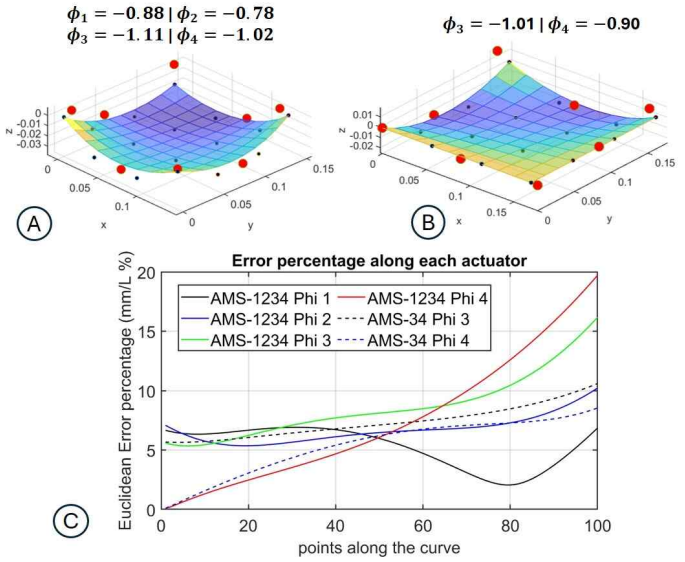

Fig. 9. (A) Negative bending of all AMS. (B) Negative Bending of AMS-3 and AMS-4. (C) Error percentage along the edges.

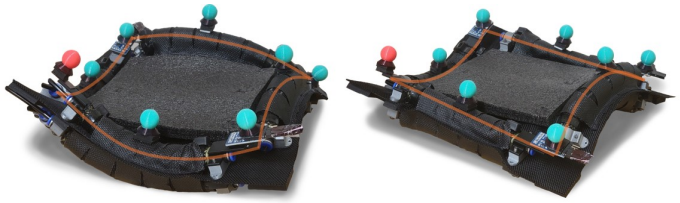

Fig. 10. Different bending directions in a single planar soft module to obtain the complex shapes

than [13]. Moreover, the shape estimation model runs at 30 Hz, which is ideal for real-time control.

Furthermore, a major contributing factor to the deviation can be identified as manufacturing and tracking errors. The kinematic model has difficulty estimating the interaction of the robot (especially the joints) with respect to the ground. However, transformations were applied to compensate for the module's resting surface.

V. Conclusions

In this work, we proposed a curve parametric-based modeling approach to estimate the shape of the soft planar module. The module was developed by arranging PMAs in a square shape on the non-stretchable fabric. The boundaries of the planar module were then used to generate the approximate shape of the surface. The proposed algorithm ran at 30 Hz and can estimate the shape with less than 12% error. The model estimated the shape of the robot with high accuracy when a single AMS was actuated. However, the model experienced difficulty when multiple AMS were actuated simultaneously. In the future, modules will be arranged in a matrix and validate the model performance.

VI. Acknowledgment

This work was supported in part by the National Science Foundation (NSF) grants IIS-2325491 (2008797), CMMI-2326536 (2048142), CMMI-2327702 (2132994), and the National Institutes of Health (NIH) R01 grant 5R01NS116148-04.

References

[1] D. D. K. Arachchige, D. M. Perera, S. Mallikarachchi, U. Huzaifa, I. Kanj, and I. S. Godage, "Soft steps: Exploring quadrupedal locomotion with modular soft robots," *IEEE Access*, vol. 11, pp. 63 136–63 148, 2023.

[2] B. Mazzolai, A. Mondini, E. Del Dottore, L. Margheri, F. Carpi, K. Suzumori, M. Cianchetti, T. Speck, S. K. Smoukov, I. Burgert *et al.*, "Roadmap on soft robotics: multifunctionality, adaptability and growth without borders," *Multifunctional Materials*, 2022.

[3] D. D. Arachchige, Y. Chen, I. D. Walker, and I. S. Godage, "A novel variable stiffness soft robotic gripper," in *2021 IEEE 17th International Conference on Automation Science and Engineering (CASE)*, 2021, pp. 2222–2227.

[4] K. Suzumori, S. Endo, T. Kanda, N. Kato, and H. Suzuki, "A bending pneumatic rubber actuator realizing soft-bodied manta swimming robot," in *IEEE Intl. Conf. on robotics and automation*, 2007.

[5] Y. Cai, S. Bi, and L. Zheng, "Design and experiments of a robotic fish imitating cow-nosed ray," *Journal of Bionic Engineering*, 2010.

[6] Z. Deng, M. Stommel, and W. Xu, "A novel soft machine table for manipulation of delicate objects inspired by caterpillar locomotion," *IEEE/ASME Transactions on Mechatronics*, 2016.

[7] O. Medina, A. Shapiro, and N. Shvalb, "Kinematics for an actuated flexible n-manifold," *Journal of Mechanisms and Robotics*, vol. 8, no. 2, p. 021009, 2016.

[8] C. Nelon, A. Shepard, I. Walker, and O. Myers, "Transverse curvature characterization of rectangular bistable cfrp laminates with a satellite capturing continuum robotic application," *Composite Structures*, vol. 325, p. 117565, 2023.

[9] C. Sansour and H. Bednarczyk, "The cosserat surface as a shell model, theory and finite-element formulation," *Computer Methods in Applied Mechanics and Engineering*, vol. 120, no. 1-2, pp. 1–32, 1995.

[10] T. Kano, Y. Watanabe, and A. Ishiguro, "Sheetbot: Two-dimensional sheet-like robot as a tool for constructing universal decentralized control systems," in *IEEE Intl. Conf. on rob. & automation*, 2012.

[11] J. Merino, A. L. Threatt, I. D. Walker, and K. E. Green, "Forward kinematic model for continuum robotic surfaces," in *IEEE/RSJ Intl. Conf. on Intelligent Robots and Systems*, 2012, pp. 3453–3460.

[12] M. Watanabe and H. Tsukagoshi, "Flexible sheet actuator that generates bidirectional traveling waves," in *2018 IEEE/ASME Intl. Conf. on Advanced Intelligent Mechatronics (AIM)*, 2018, pp. 328–333.

[13] H. Habibi, C. Yang, I. S. Godage, R. Kang, I. D. Walker, and D. T. Branson III, "A lumped-mass model for large deformation continuum surfaces actuated by continuum robotic arms," *Journal of mechanisms and robotics*, vol. 12, no. 1, p. 011014, 2020.

[14] R. J. Webster III and B. A. Jones, "Design and kinematic modeling of constant curvature continuum robots: A review," *The Intl. Journal of Robotic Research*, vol. 29, no. 13, pp. 1661–1683, 2010.

[15] I. S. Godage, G. A. Medrano-Cerda, D. T. Branson, E. Guglielmino, and D. G. Caldwell, "Modal kinematics for multisection continuum arms," *Bioinspiration & biomimetics*, vol. 10, no. 3, p. 035002, 2015.

[16] D. D. Arachchige and I. S. Godage, "Hybrid soft robots incorporating soft and stiff elements," in *IEEE Intl. Conf. on Soft Robotics (RoboSoft)*, 2022, pp. 267–272.

[17] D. M. Perera, D. D. Arachchige, S. Mallikarachchi, T. Ghafoor, I. Kanj, Y. Chen, and I. S. Godage, "Teleoperation of soft modular robots: Study on real-time stability and gait control," in *IEEE International Conference on Soft Robotics (RoboSoft)*, 2023, pp. 01–07.

[18] G. Hu, J. Wu, and X. Qin, "A novel extension of the bézier model and its applications to surface modeling," *Advances in Engineering Software*, vol. 125, pp. 27–54, 2018.

[19] M. Khan, "cubic bezier least square fitting," https://www.mathworks.com/matlabcentral/fileexchange/15542-cubic-bezier-least-square-fitting, 2024, [Online; accessed January 20, 2024].